UNIVERSITY OF
BIRMINGHAM

University of Birmingham
Research at Birmingham

Laser powder bed fusion of Ti-rich TiNi lattice structures

Tan, Chaolin; Li, Sheng; Essa, Khamis; Jamshidi, Parastoo; Zhou, Kesong; Ma, Wenyou; Attallah, Moataz M.

DOI:
10.1016/j.ijmachtools.2019.04.002

License:
Creative Commons: Attribution-NonCommercial-NoDerivs (CC BY-NC-ND)

Document Version
Peer reviewed version

Citation for published version (Harvard):
Tan, C, Li, S, Essa, K, Jamshidi, P, Zhou, K, Ma, W & Attallah, MM 2019, 'Laser powder bed fusion of Ti-rich TiNi lattice structures: process optimisation, geometrical integrity, and phase transformations', *International Journal of Machine Tools and Manufacture*, vol. 141, pp. 19-29. https://doi.org/10.1016/j.ijmachtools.2019.04.002

Link to publication on Research at Birmingham portal

Publisher Rights Statement:
Checked for eligibility: 03/04/2019

General rights
Unless a licence is specified above, all rights (including copyright and moral rights) in this document are retained by the authors and/or the copyright holders. The express permission of the copyright holder must be obtained for any use of this material other than for purposes permitted by law.

•Users may freely distribute the URL that is used to identify this publication.
•Users may download and/or print one copy of the publication from the University of Birmingham research portal for the purpose of private study or non-commercial research.
•User may use extracts from the document in line with the concept of ‘fair dealing’ under the Copyright, Designs and Patents Act 1988 (?)
•Users may not further distribute the material nor use it for the purposes of commercial gain.

Where a licence is displayed above, please note the terms and conditions of the licence govern your use of this document.

When citing, please reference the published version.

Take down policy
While the University of Birmingham exercises care and attention in making items available there are rare occasions when an item has been uploaded in error or has been deemed to be commercially or otherwise sensitive.

If you believe that this is the case for this document, please contact UBIRA@lists.bham.ac.uk providing details and we will remove access to the work immediately and investigate.

Download date: 27. Apr. 2024

Laser Powder Bed Fusion of Ti-rich TiNi Lattice Structures: Process Optimisation, Geometrical Integrity, and Phase Transformations

Abstract: The use of Laser Powder Bed Fusion (LPBF) in fabricating TiNi-based lattices enables tailoring the mechanical and physical properties of the structure, in addition to the functionality associated with the shape-memory effect. In this work, TiNi lattice structures were fabricated using LPBF, following an optimisation study for LPBF parameters investigating the geometrical integrity of the lattices, microstructural evolution, and phase transformation behaviour. A process map for TiNi lattices was constructed to visualise the influence of LPBF parameters on the build density, elemental evaporation, and impurity pick-up. The optimum LPBF processing window was found to be ~60-90 J/mm^3 volumetric energy density, achieving >99% relative density. Optimisation of the geometrical integrity of the LPBF-fabricated lattices, including the pore and strut sizes, was performed by considering the influence of the laser track width (LTW), beam compensation (BC), and contour distance (CD). As a result, when CD-BC=LTW/2, the deviation in strut size from the target design size was reduced to <2%. The build microstructure was affected by LPBF parameters, where the dendritic cell size increased with the increase in LPBF heat input, also resulting in a change in the solidification structure morphology from cellular to columnar dendritic structures. The phase transformation behaviour was investigated using Differential Scanning Calorimetry to understand the effect of LPBF parameters on the formation of Ti_2Ni intermetallics and impurity pick up (oxygen and carbon), and the resulting impact on the phase transformation temperatures.

Keywords: Laser Powder Bed Fusion; Shape Memory Alloys; Lattices; Phase Transformations

1. Introduction

There is a growing interest in additive manufacturing (AM) of TiNi shape memory alloys (SMAs), as they provide an interesting combination of functional performance due to the shape memory effect (SME), as well as unique mechanical and physical properties (e.g. low elastic modulus, biocompatibility [1, 2], mechanical strength, and excellent corrosion and wear resistance [3, 4]). They have been employed in biomedical implants and devices [5], aerospace components [6], and functional devices [7]. TiNi components are typically processed via casting, powder metallurgy (PM), wire drawing, and machining [5, 8]. Vacuum casting is essential to avoid increasing the impurity levels (O, C, and N), which could generate TiC, TiO_2, and $Ti_4Ni_2O_X$ secondary phase particles, which degrade the functional and mechanical properties of TiNi SMAs [4, 8]. PM will also result in impurity pick-up, and is limited in its geometrical complexity [2]. Machining of TiNi encounters significant tool wear owing to the intrinsic mechanical behaviour of SMAs, making it essential to use special machining processes (e.g. laser micro-machining for stents) [9]. Thereby, traditional manufacturing methods appear to hinder the performance and applications of TiNi SMAs.

Laser powder bed fusion (LPBF) produces parts in a layer-wise incremental manner using a laser to melt and consolidate thin layers of powders [10, 11], providing an alternative approach to circumvent the challenges associated with traditional manufacturing methods of TiNi. Due to its localised heating and rapid cooling rates (up to 10^6 K/s), LPBF can reduce chemical segregation, cause grain refinement, and improve the mechanical behaviour [12]. Besides, LPBF provides design freedom and flexibility, making it an ideal process for the fabrication of structures with engineered porosity like lattices, auxetics, and other complex functional structures [13].

However, LPBF of TiNi encounters a number of challenges, including the formation of structural defects (pores, cracks, or lack of fusion), selective Ni-evaporation, pick-up of impurity elements, and the formation of intermetallic particles, which affect the phase transformation temperatures, mechanical behaviour and functional properties [5, 12, 14]. Previous process optimisation studies identified an optimum LPBF energy density window of ~52-83 J/mm^3 [15-18], but that was mainly for solid and Ni-rich TiNi-alloys, which as such may be not suitable for LPBF of Ti-rich TiNi lattice structures. When fabricating lattices by

LPBF, the laser exposure area in each layer is mostly made up of single laser tracks and is significantly reduced, compared with fabricating solid/bulk structures. As a result, the heat transfer and solidification mechanism are also quite different compared with bulk structures. However, specific studies on LPBF optimisation for TiNi lattices are fairly limited, especially studies that considered process optimisation for porosity, elemental evaporation, cracking, intermetallic precipitation, impurities pick-up, and the resulting phase transformation behaviour, simultaneously.

The geometrical integrity of LPBF-fabricated lattices can be expressed in terms of the strut size and structural porosity (i.e. lattice nominal density), compared with the target design. Depending on the process parameters, two aspects are known to cause the deviation between the target design and the LPBF-produced geometry. The first aspect is the residual partially melted powders that form on the struts, which result in a larger strut diameter and a higher nominal density. Arabnejad *et al.* [19] found that the pore size within the lattice is typically smaller than the target design, generating a large disparity in the structural porosity. Furthermore, the size of the inclined struts typically ends up becoming larger than the target design due to the staircase-effect associated with building inclined geometries. The second aspect is the influence of the laser thermal footprint (as opposed to the optical footprint), as depicted in Fig. 1a, which results in a larger laser track width (LTW) than the laser spot size. Some studies investigated the utility of post-processing methods to remove the residual powder by post-treatments, such as chemical etching, electro-polishing, and sandblasting [20, 21]. Nonetheless, no reports have been published to-date on controlling the lattice geometry using laser beam compensation strategies, which could be an intrinsic way to efficiently reduce the variability in the geometrical integrity. Normally, the laser compensation strategies involve tailoring the laser beam compensation (BC) and contour distance (CD). As illustrated in Fig. 1b, BC (also known as the beam offset) is the distance between the border of the laser filling scan area and the defined real part edge, while the CD represents the distance from the centre of the contour scan track, which is usually employed to improve the surface finish, to the target design edge. Optimising the BC and CD ensures that LPBF-fabricated lattices are not oversized by compensating for the width of the contour track melt pool. This is analogous to compensating for the machine tool diameter in machining.

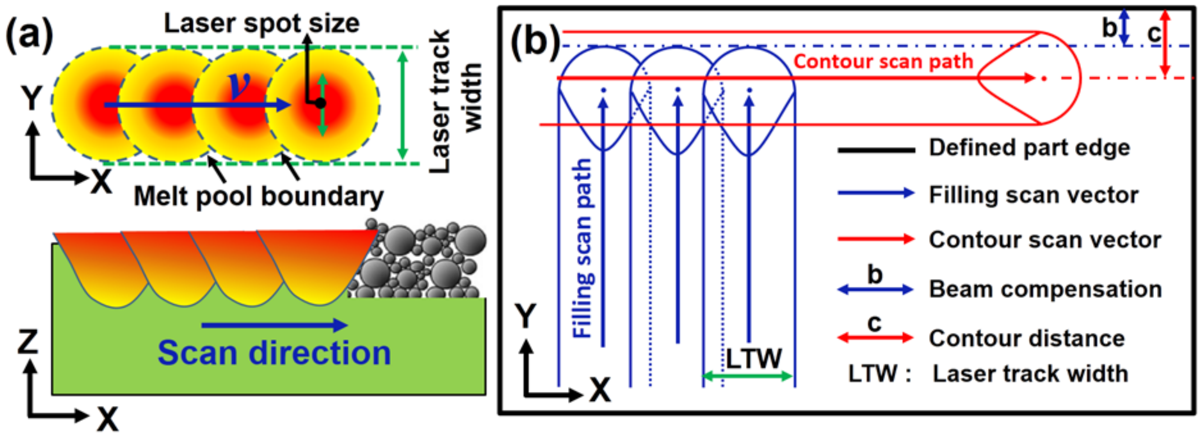

Fig. 1. Schematic illustrations for (a) the laser track width, and (b) laser filling strategies, illustrating the definition of the beam compensation (BC) and contour distance (CD).

Aiming to develop high-performance TiNi for medical implants, Ti-rich TiNi was selected for this study due to their low elastic modulus, and the reduced Ni-content to avoid the adverse (allergic) effects of Ni-ion release [22]. Potentially, LPBF may enhance the biocompatibility through the formation of a TiO_2-based oxide film covering the surface of TiNi struts [23] to reduce the toxicity and Ni-ion release well below the cytotoxic concentration [24]. In this work, LPBF parameters were optimised considering the aforementioned factors to construct a process map of TiNi lattices. The lattice geometrical integrity, microstructural evolution, and phase transformation behaviour were also assessed.

2. Material and Experimental Methods

2.1. Materials and Processing

Argon atomised pre-alloyed $Ti_{54.8}Ni_{45.2}$ (at. %) powder, with a size distribution range of 20-50 μm, was supplied by TLS Technik GmbH & Co (Germany). The powder was used for LBPF processing and powder hot isostatic pressing (HIP). The morphology and microstructure of the powder were characterised using a Hitachi TM3000 Scanning Electron Microscope (SEM).

Lattices were built using a Concept Laser M2 Cusing LPBF system, with a protective Argon atmosphere, controlled down to 100 ppm O_2, and employing a continuous wave fibre laser with a nominal maximum output power of 400 W and a focus diameter of ~75 μm. A hatch distance (h) of 75 μm was used, which is similar to the laser spot diameter. Taking the mean particle size of the powder into account, a layer thickness (t) of 30 μm was selected. In order to achieve fully dense parts, an optimisation study involving the laser parameters (laser power (P) and scan speed (*v*)) was performed in the ranges of 60-120 W and 150-600 mm/s, respectively. To describe an equivalent value for the heat input, the volumetric energy density (E_v) was used, as defined as $E_v=P/(v\times h\times t)$ [25]. The laser was scanned in a continuous raster pattern with 'meander on' and 0.1 ms corners delay. The laser scanning direction rotated in 90º between the subsequent layers.

HIP was performed in an EPSI hot isostatic press to obtain fully dense TiNi as a density reference. TiNi powder was encapsulated in a mild steel can, and HIPed at 1000 ºC for 3 hours under a pressure of 100 MPa.

2.2. Characterisation

Archimedes density measurements for the HIPed and LPBF-fabricated TiNi samples was performed using an OHAUS Adventurer® Analytical balance using pure ethanol according to ASTM B962-08. The porosity within the builds was measured using ImageJ® image analysis software from ten micrographs, which were captured at 25× magnification on a Brunel optical microscope (OM). A JOEL 6060 W-filament SEM fitted with an Oxford Energy Dispersive Spectrometer (EDS) was used to observe the surface morphology, as well as to measure the elemental composition of the specimens. X-ray diffraction (XRD) was conducted using a Bruker D8 Advance Diffractometer with a Cu Kα radiation (wavelength, λ= 0.15418nm), operated at 40 kV and 40 mA using a step size of 0.02° at room temperature. Ti_2Ni phase volume fractions were quantified using ImageJ® from BSE micrographs of polished samples. To analyse the microstructure in the X-Y plane (normal to the build direction), Kroll's reagent (2%HF+10%HNO_3+88%H_2O) was used. The content of impurity elements (carbon, oxygen, and nitrogen) in the powder and LPBF-processed samples was also determined using a LECO TC436AR analyser. Phase transformation temperatures (TTs) of the powder and the as-fabricated specimens were identified using a Mettler-Toledo DSC1 Differential Scanning Calorimetry (DSC) system. The specimens were thermally cycled between -10˚C and 120 ˚C, at a heating/cooling rate of 10˚C/min in an Ar atmosphere. No differences in the TTs were noticed in the DSC traces with repeated thermal cycling.

3. Results

3.1. Powder and Lattice Characteristics

The external morphology and cross-sectional microstructure of the powder are shown in Fig. 2. The powder was generally spherical, with limited satellite particles as shown in Fig. 2a, which was reflected in a good spreading during LPBF. The cross-section of powder (Fig. 2b) showed a cellular microstructure, with a dark grey phase on the cell boundaries. EDS analysis showed that the dark phase along the cell boundaries is Ti-rich, which was identified as the intermetallic compound Ti_2Ni, with the surrounding light grey phase being TiNi, according to the Ti-Ni phase diagram and as identified in other studies on LPBF of TiNi [12, 26]. The main impurity elements in the powder (O, C, and N) were measured to be 1250 ppm, 427 ppm, and 130 ppm, respectively.

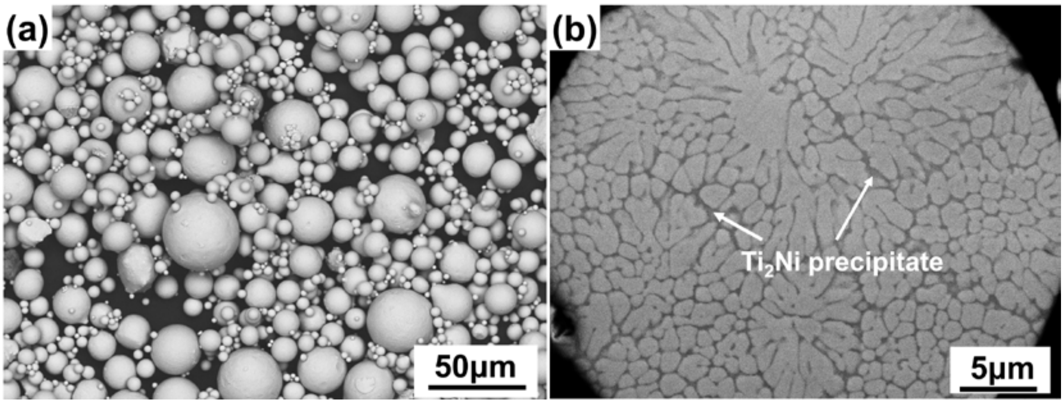

Fig. 2 SEM micrographs for the TiNi powder, showing: (a) powder morphology, and (b) cross- section microstructure.

Lattice structures for bone replacement should meet the criteria of pore interconnectivity to promote cell migration, proliferation and differentiation, in order to enable nutrient-waste exchange and enhance bone ingrowth (osseointegration) [27]. Bone ingrowth requires the pore size to be 50-800 μm, with a structural porosity > 50% [19, 28, 29]. As shown in Fig. 3a, a diagonal cubic structure (also referred to as skeletal structure) was designed since it has no overhangs (i.e. suitable for self-support during LPBF) and shows strong geometrical isotropy. The target design unit cell size, strut thickness, and pore size were 1000 μm, 310 μm, and 400 μm, respectively. A cuboid lattice with a size of 8 × 8 × 12 mm^3 was used in this study. The structural porosity % (P_S) of the sample was calculated as the percentage of the voids volume to the fully solid volume as:

$$P_S = \left(1 - \frac{V_L}{V_S}\right) \times 100\%$$

where V_L is the volume of the lattice unit cell and V_S is its enclosing volume (L^3). The structural porosity of this diagonal cubic unit cell is 55 %, so the relative density is 45%. The LPBF-fabricated samples are shown in Fig.3b. It is important to note that higher energy density promoted the tendency to block and/or disfigure the pores, with the pore morphology being more recognisable and uniform in the specimens that were built using low energy density conditions.

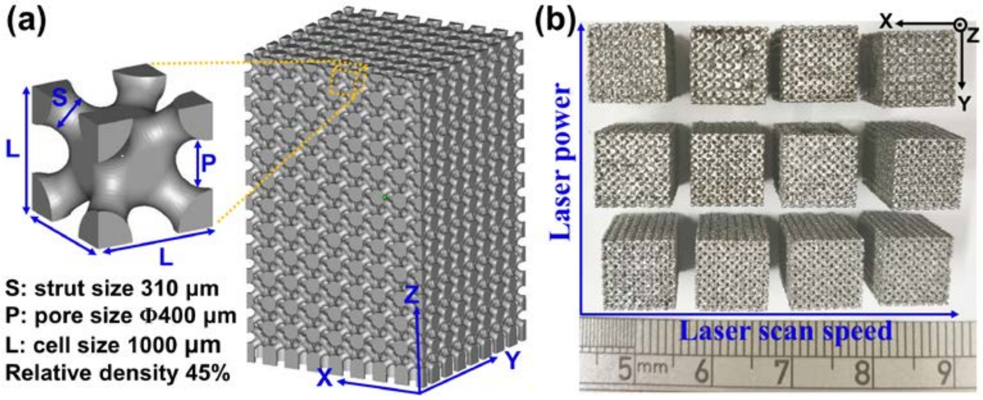

Fig. 3. The geometry of the TiNi lattice, showing: (a) isometric view of the unit cell and the full lattice, and (b) LPBF-fabricated lattices, with a well-defined pore morphology for the low P builds (bottom row), compared with a more disfigured pore morphology for the high P builds (top row).

3.2. Parameters optimisation

3.2.1. Surface/Pore Morphology

The horizontal (X-Y) surface morphologies of the lattices produced using different laser parameters are shown in Fig. 4. Due to the nature of LPBF as previously explained, the lattice surface contains some partially melted residual powder particles attached to the struts. As shown in Fig.4a-d, increasing the E_v from 67 J/mm^3 to 178 J/mm^3 resulted in higher levels of densification, causing the pores to be blocked, and resulting in a more dense structure. This is attributed to the increase in strut size, ultimately reducing the pore size, due to the larger melt pool width at higher E_v conditions[30]. Besides, as revealed in Fig. 4f, at the same E_v, higher

P conditions result in a reduction in the pore size, presumably also due to the wider melt pool. Interestingly, decreasing the E_v from 67 J/mm^3 to 44 J/mm^3 also resulted in a slight decrease in the pore size, or rather its geometrical definition, as well as slightly increasing the strut size, comparing the morphologies of Fig. 4d with Fig. 4e. This can be attributed to the balling effect, which occurs at low E_v conditions due to insufficient wetting by the molten liquid [11, 31]. Balling increases the surface roughness and leads to more powder attachment to the surface of the struts.

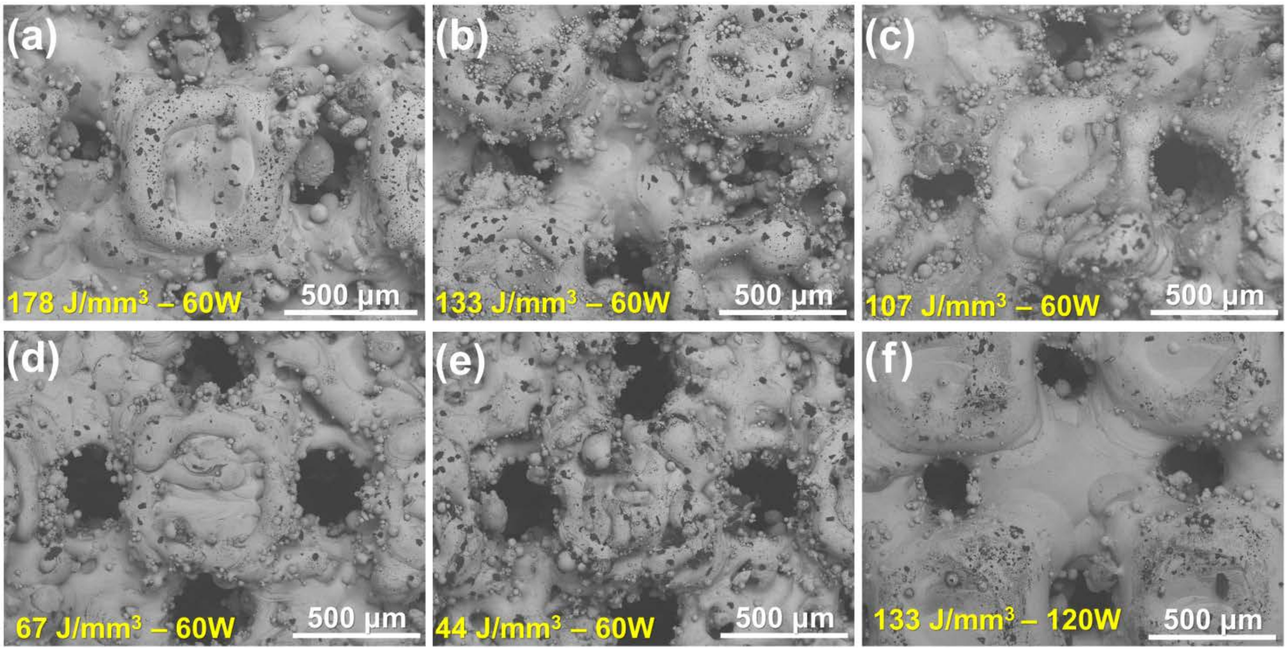

Fig. 4. Surface morphologies of LPBF-fabricated samples using different build parameters.

3.2.2. Defects and densification

The Archimedes density of the HIPed sample was measured as 6.219±0.005 g/cm^3, with a relative density of ~99.93±0.03% according to the measured porosity. As such, a fully dense (defect-free) structure of the investigated TiNi-alloy has a theoretical density of 6.223 g/cm^3, which was used as a reference for the LPBF-processed samples. The variation in the Archimedes density of the lattices versus E_v is plotted in Fig. 5. Overall, the samples produced using E_v of 67-133 J/mm^3 had a relatively higher density, among which the 90W / 80J/mm^3 sample achieved the highest density of 6.208±0.007 g/cm^3 (99.76% of the theoretical density). Lowering E_v from 67 J/mm^3 or further increasing E_v from 133 J/mm^3 resulted in a density reduction. It should be noted that the samples produced using 90 W achieved a higher density than those with 60 W and 120 W, at the same E_v of 133 J/mm^3. To further investigate the densification behaviour, the cross-sections of struts were observed using OM. Representative images showing the defects were correlated with E_v and Archimedes density, Fig. 5. The morphology of the sample produced using 44 J/mm^3 showed irregular pores with unconsolidated particles, which is characteristic of lack of fusion defects caused by insufficient heat input [14]. At E_v of 267 J/mm^3, the sample exhibited a significant number of spherical pores, which is characteristic of keyhole defects [32, 33]. In contrast, the sample produced at 67 J/mm^3 showed few fine pores, which resulted in a higher relative density. Besides, high P increases the tendency of keyholing, the P=120 W processed sample has more keyhole defects than that of 60 W condition despite using the same E_v, 133 J/mm^3. Cracks were present in all the high power conditions (P=90 W and 120W), and also in some low power conditions (P=60 W and 75W), as well as in high E_v conditions (≥133 J/mm^3). The cracks were aligned normal to the build direction along the X-Z and Y-Z planes causing interlayer delamination due to the residual stresses along the build direction, and initiating from the Ti-rich inter-dendritic regions [12].

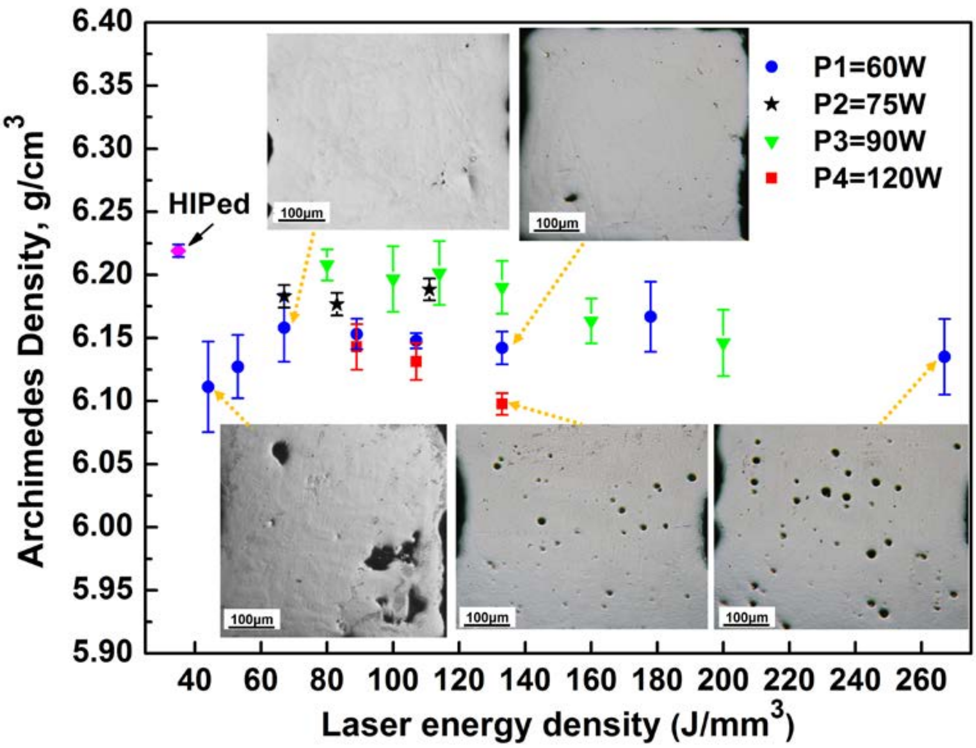

Fig. 5. Effect of the volumetric energy density on the density and defect types in the LPBF-fabricated samples.

3.2.3. Evaporation and Impurity

Selective elemental evaporation is known to occur during LPBF, especially under high laser energy input, resulting in higher evaporation rates for the lower boiling point elements within an alloy [5]. In TiNi-LPBF, Ni is likely to evaporate more readily than Ti, since Ni has a vaporisation enthalpy 374.8 kJ/mol and a boiling point of 2913˚C, compared with 425.5 kJ/mol and 3287˚C for Ti. The Ni-content of the samples produced in this study was quantified using several large area EDS measurements, as shown in Fig. 6a. It was found that Ni-evaporation in low P (P=60 W) and low E_v ($\leq$90 J/mm^3) conditions was negligible. Nonetheless, Ni-loss became rather intensive in higher P and/or higher E_v conditions. Moreover, at $E_v \geq 200$ J/mm^3, Ni-loss exceeded 1 at. % even in low P condition (P=60W). Furthermore, in high P conditions (P=120 W), Ni-loss was >1 at. % even when the E_v was merely 133 J/mm^3. From a correlation perspective, Ni-loss increased with the increase in P at the same E_v, and generally increased with the increase in E_v.

In addition to selective vaporisation, LPBF is known to increase the susceptibility for impurity elements pick-up from the surrounding atmosphere, despite the inert atmosphere. As revealed in Fig. 6b, the impurity pick-up (O, N, and C) varied depending on the laser energy input. At lower E_v, the impurity pick-up was insignificant in comparison to the original powder. However, at elevated P and E_v, impurity pick-up increased. Similar observations were found in other studies on LPBF-processing of TiNi [16]. It is important to note that the combined effect of Ni-loss and impurity elements pick-up significantly affects the phase transformation behaviour in TiNi-based SMAs, potentially disturbing the alloy performance.

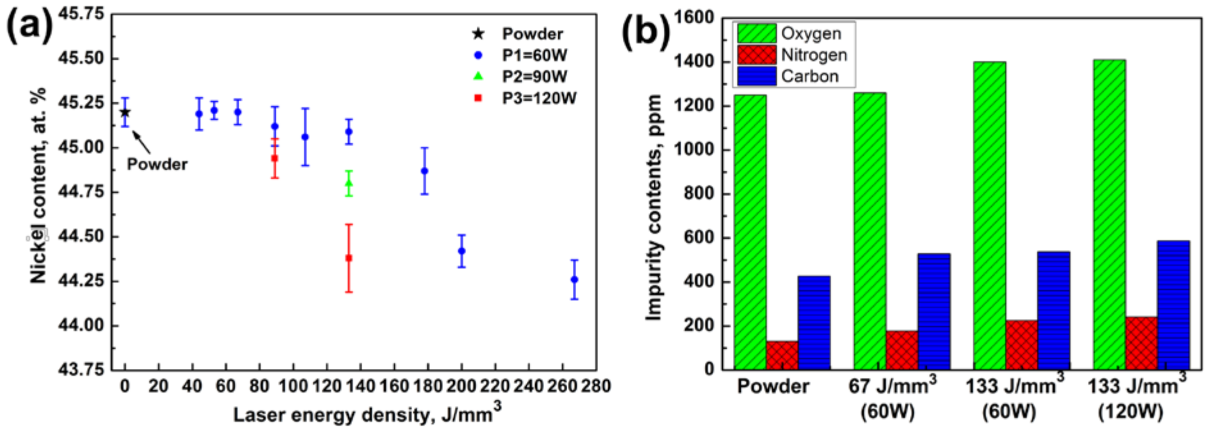

Fig. 6. Effect of laser parameter on the nickel evaporation (a) and impurity pick-up (b).

3.3. Geometrical Integrity

3.3.1. Effect of LPBF parameters on the laser track width

As shown in Fig. 4 and Fig. 5, in the lattice sample (67 J/mm^3) that achieved the least build defects, the average pore size (317±17μm) was still significantly smaller than the design value of 400 μm (Fig. 3), which suggested that a further geometrical refinement study was needed. The effect of LPBF parameters on the laser track width (LTW) was investigated in Fig. 7 by building single-track walls using a range of parameters. Fig. 7a shows representative micrographs for the laser tracks associated with different P and E_v. LTW measurements using SEM images are plotted in Fig. 7b. It is obvious that the LTW increased with increasing P and E_v. At the same E_v of 133 J/mm^3, higher P (120 W) resulted in significantly larger LTW than lower P (60 W), Fig. 7a. Moreover, it is notable that increasing E_v reduces the tendency to have partially melted residual powder particles stuck on the strut surfaces, as a result of the reduction in balling due to the improved wetting. Besides, increasing P seems to aggravate the sticking of residual particles on the surface, at the same E_v condition, similar to the results reported by Qiu *et al.* [34]. The LTW at the optimum E_v condition (67 J/mm^3) was determined to be 93±5 μm. Knowing the LTW at the optimum E_v condition is essential for the laser compensation strategies, as it will be shown in the following section.

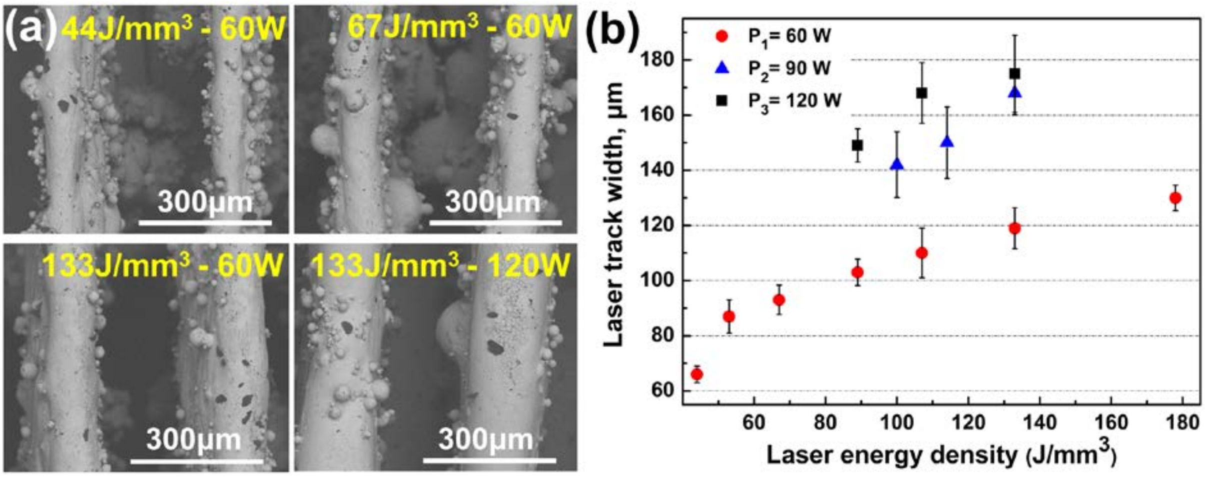

Fig. 7. (a) SEM micrographs showing the morphology of individual laser tracks produced with different process parameters, and (b) the relationship between E_v and P and the LTW.

3.3.2. Laser beam compensation optimisation

In order to understand the effect of BC on the geometrical precision, lattice samples with different BC values were fabricated using the optimum E_v of 67 J/mm^3 without a contour scan.

SEM micrographs for samples produced with BC values of 0 µm, 25 µm, 50 µm and 75 µm are shown in Fig. 8a-d. It is obvious that increasing the BC increases the pore size, while reducing the strut size and decreasing the nominal density of lattices, Fig. 8e. At BC of 0 µm, the pore size was the smallest, while the strut size was the largest in the investigated conditions, deviating from the design values, which suggests that a tailored BC is needed to achieve geometrical precision. In contrast to BC=0 µm, at BC=75 µm, the pore size becomes larger, while the strut size becomes smaller than the design values. BC=25 µm was the optimum value for geometrical precision in the absence of a contour scan, since the deviations in the pore and strut were only ~4% from the design value. Nonetheless, in the absence of a contour scan, partially melted powder particles were attached to the surface, with the edges being quite uneven. This implies that a contour scan is essential for improving the edge quality and surface integrity.

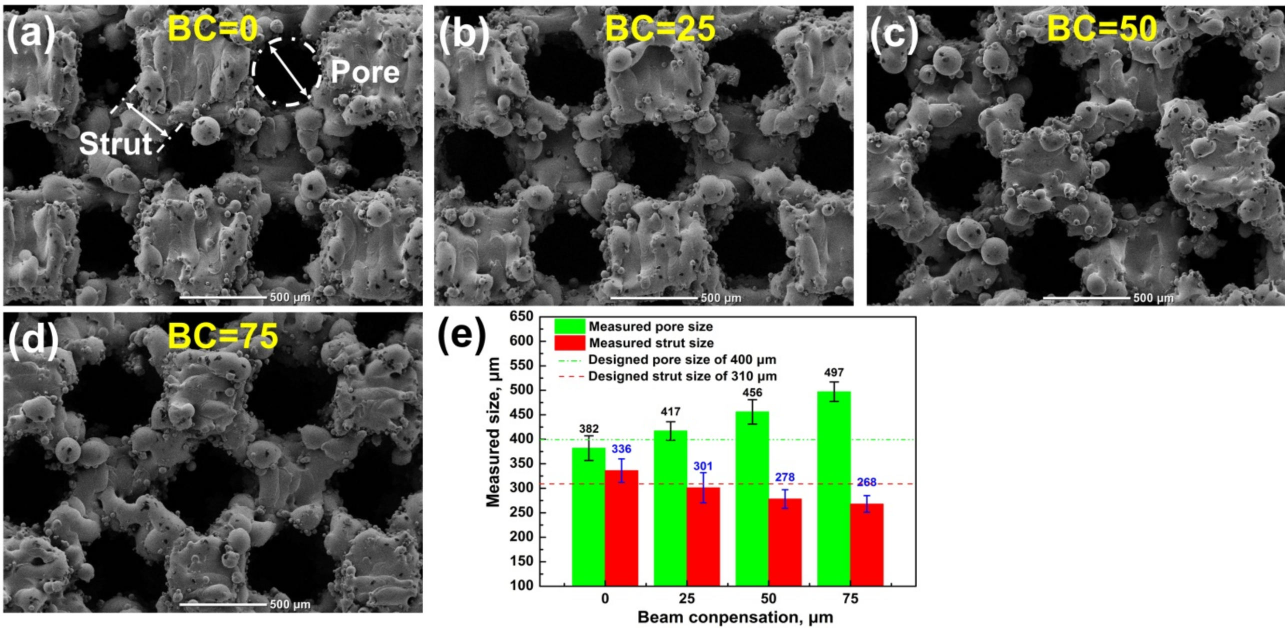

Fig. 8. Effect of laser BC on the pore size and strut size: (a) - (d) SEM micrographs for the samples built using BC of 0, 25, 50, and 75 µm, respectively; and (e) the relationship between BC and pore size and strut size (average 15 measurements from different SEM micrographs).

3.3.3. Laser beam compensation and contour distance optimisation

The combined effect of BC and CD on the lattice geometrical integrity is shown in Fig. 9a. All the samples were produced using the same E_v of 67 J/mm^3. At BC = 25 µm, the pore size significantly increased from 313 μm to 440 μm by increasing the CD from 0 to 100 μm. The same correlation occurred at BC = 50 μm. Interestingly, using equal BC and CD values, the pore size increased when they were increased from 25 μm to 75 μm, as summarised in Fig. 9b. Overall, enlarging the gap between the CD and BC values can increase the pore size while reducing the strut size. Further analysis reveals that a variation of CD has a more significant impact on the lattice geometry than BC, since at a constant CD of 75 μm, increasing BC had a slight influence on the enlargement of pore size. As noted from Fig. 9b, samples processed using BC=25 μm along with CD=75 μm had the best geometrical precision with a reduced deviation of <2% in strut and pore sizes in comparison to the target design sizes, in addition to enhancing the circularity of the pores.

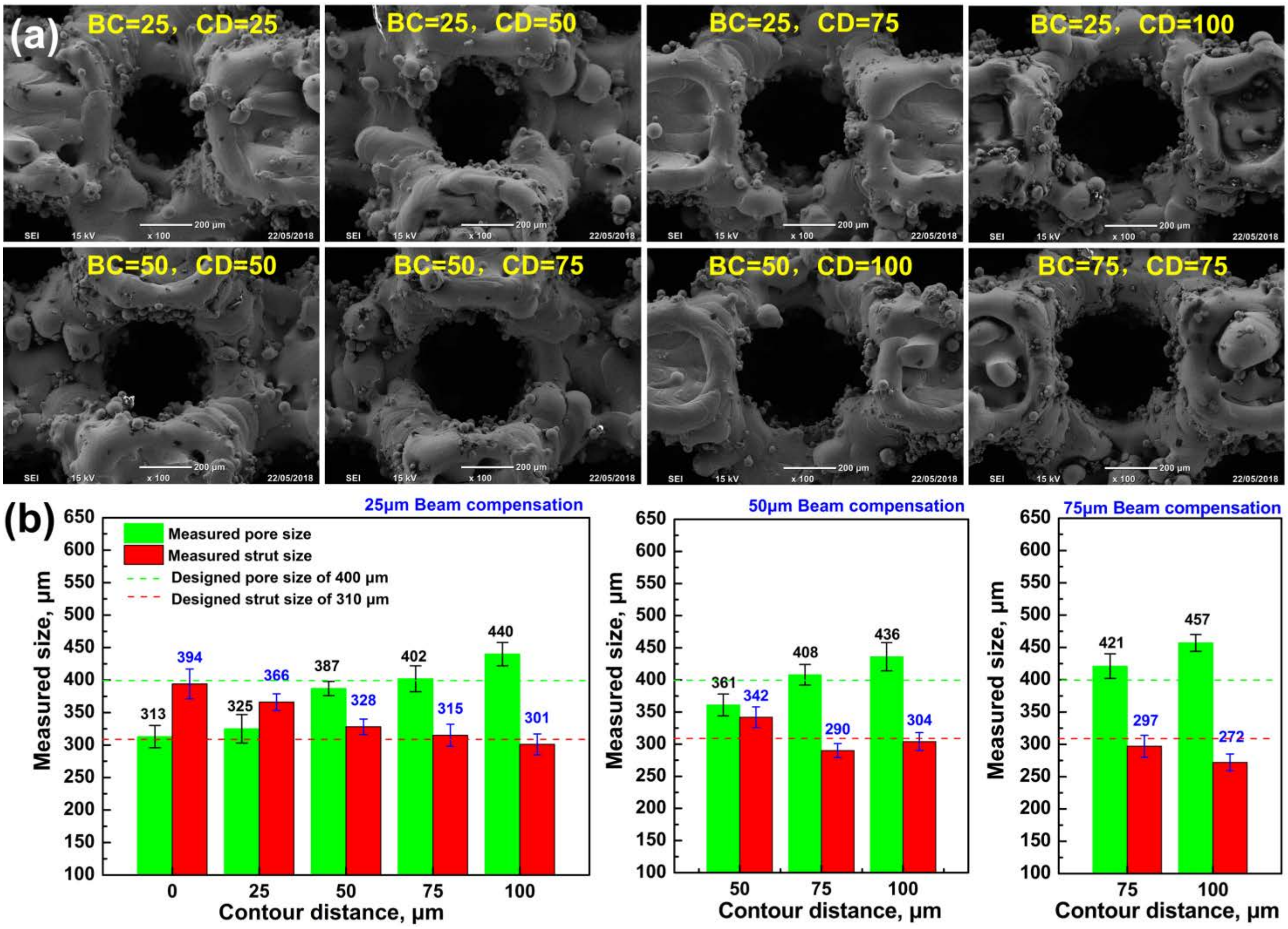

Fig. 9. The combined effect of beam compensation (BC) and contour distance (CD) on the lattice geometrical integrity: (a) SEM micrographs showing the pore morphology at different BC and CD values, and (b) deviations in the pore size and strut size between the LPBF-fabricated lattice and the design value at difference BC and CD.

3.4. Microstructural observation

Fig. 10 shows the as-fabricated microstructure in the LPBF-fabricated lattices using different process parameters. Generally, the solidification cell size/dendrite arm spacing (DAS) increased with the increase in E_v. Besides, the microstructural morphology of the solidification structure varied depending on the E_v. Rounded fine cellular structures (Fig. 10a, b, and c) were prevalent in lower P and E_v conditions, while columnar and coarser cellular structure (Fig. 10d, e, and f) were more predominant in higher power and E_v processed samples. It is known that the temperature gradient G (K/m) and growth rate R (m/s) during solidification control the morphology and size of the solidified microstructure (e.g. DAS). The G/R ratio determines the solidification mode, while the product of G × R indicates the cooling rate (K/s) that controls the size of the solidified microstructure [35, 36].

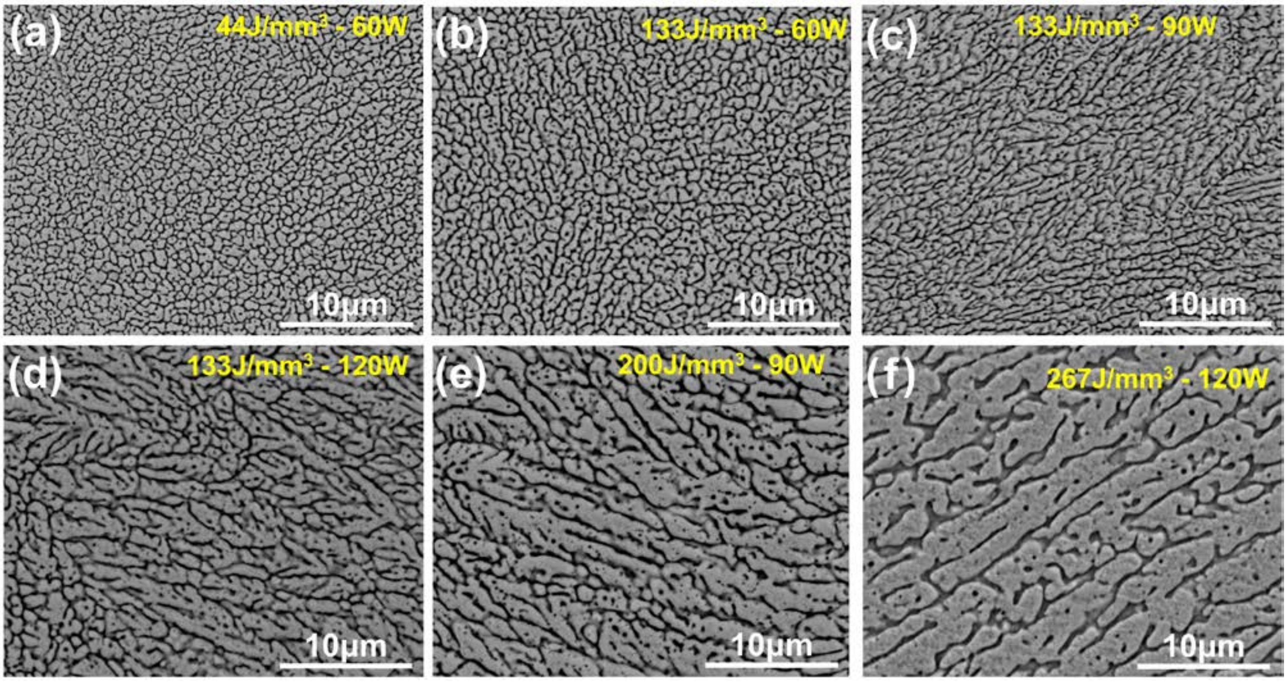

Fig. 10. SEM micrographs of the microstructures in LPBF-fabricated TiNi samples processed using different E_v and P conditions.

At low E_v, which is associated with high laser scan speed, G increases, which in turn increases the nucleation and formation of the fine cells/dendrites. At high E_v, the melt pool is exposed to higher temperatures, which slows the solidification rate [37, 38]. The growth modes are generally defined as planar, cellular, columnar dendrites, and equiaxed dendrites. The planar growth needs to satisfy the following criterion [35]:

$$\frac{G}{R} \geq \frac{\Delta T}{D_L}$$

where $\Delta T = T_L - T_S$ is the equilibrium freezing range, D_L is the diffusion coefficient of the solute in the liquid. When increasing the E_v, G decreases, which alters the solidification mode from planar growth to columnar dendrites gradually. As discussed previously, the solidification structure coarsens with the increase in P, at a constant E_v (Fig. 10 c and d), since higher P appears to have a more significant effect on increasing the melt temperature and temperature gradient than the laser scan speed [39]. The melt pool size and fusion boundary width are smaller in lower energy input, which results in a higher cooling rate [40].

XRD patterns of the powder and LPBF-fabricated TiNi samples confirm constitutions of Ti_2Ni and TiNi phases, Fig. 11a. Different E_v and P processed samples have the same peak positions, but the peak intensities seem different. For example, the 42.5° peak of TiNi phase in 267 J/mm^3 fabricated sample seems to be much weaker than that of the powder and low E_v processed samples, 44 J/mm^3 for instance. The variable peak intensity implies the process parameters also affected the volume fraction of the interdendritic intermetallic phase Ti_2Ni. Restricted by the overlapped peaks of those two phases (e.g. the peaks at ~41.5° and 45.5°), quantifying the phase contents by XRD peaks was not straightforward. Meanwhile, it is notable in Fig. 10 that interdendritic Ti_2Ni volume fraction increased with the increase in E_v. As illustrated in Fig. 11b, the differences in contrast between Ti_2Ni (dark) and TiNi (grey) are distinct. Image analysis from BSE micrographs of polished samples was performed to measure the Ti_2Ni phase volume fractions. The results are summarised in Fig. 11c. The powder has a Ti_2Ni vol.% of about 18%, similar to the low E_v produced samples (such as 44 and 67 J/mm^3), which had the same Ti_2Ni friction level as in the powder, suggesting that the cooling rates associated with these conditions are similar to the cooling rates associated with gas atomisation. Higher E_v levels led to an increase in the Ti_2Ni content dramatically, with the sample processed at 267 J/mm^3 having a Ti_2Ni vol. % of 27%. Interestingly, the Ti_2Ni vol. % in the HIPed sample (about 26%) is comparable to the high E_v samples and is significantly higher than in the powder, as the extended hold at 1000 ˚C during HIPing and the subsequent slow cooling promoted the precipitation of Ti_2Ni. In general, high Ti_2Ni content has negative effects on the performance of TiNi. On one hand, the Ti_2Ni is very brittle, which is known to promote cracks formation along the continuous Ti_2Ni phase along the interdendritic regions. On the other hand, high Ti_2Ni content impairs the SE behaviour and SME as it disturbs the TiNi matrix chemistry, and accordingly the phase transformation behaviour [12].

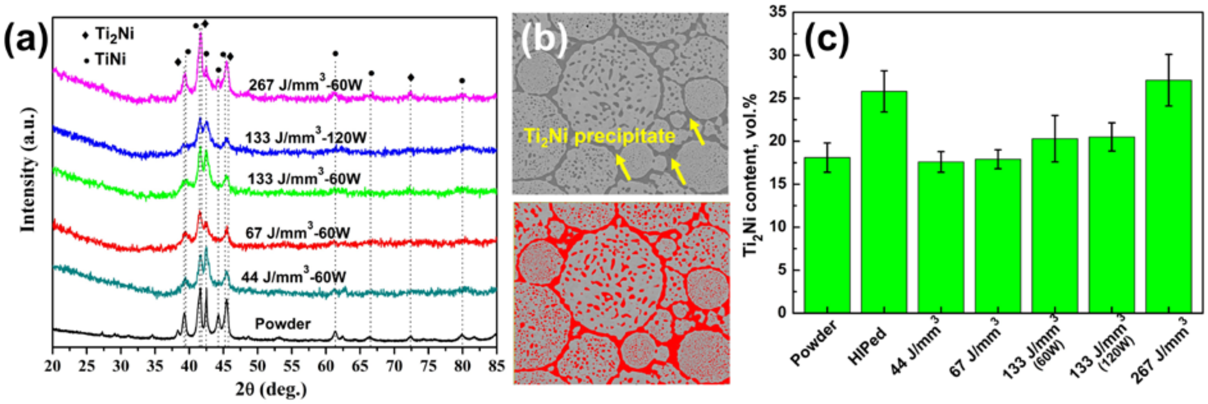

Fig. 11. (a) XRD patterns of LPBF-fabricated TiNi samples processed using different E_v and P conditions, (b) illustration showing image analysis of Ti_2Ni fraction content, and (c) Ti_2Ni volume fraction in the powder, HIPed and LPBF samples.

3.5. Phase transformation behaviour

Fig. 12 shows the DSC traces for the powder and LPBF-processed TiNi samples, which demonstrate the variation in the phase transformation temperatures (TTs), as a function of E_v and P. The TTs are also summarised in Table 1. Overall, the austenite finish temperature (A_f) and martensite start temperature (M_s) of LPBF-processed samples decreased in comparison to the powder. Additionally, increasing E_v and P resulted in decreasing the A_f and M_s. Specifically, the increase of E_v from 67 J/mm^3 to 267 J/mm^3 caused a decrease of about 9˚C and 5˚C for the A_f and M_s, respectively. The changes in TTs were correlated to the Ni-loss, impurities pick-up, and intermetallics contents. Ni-loss data (Fig. 6a) suggested that the Ni contents in different laser parameter processed samples are different; the impurity (C, N, and O) level (Fig. 6b) and Ti_2Ni intermetallic content (Fig. 11c) of samples also vary depending on the laser parameters.

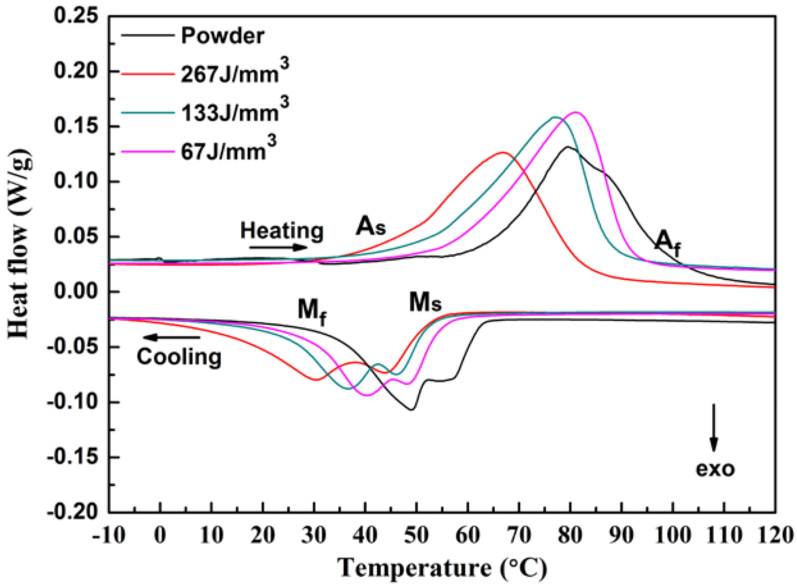

Fig. 12. DSC traces for the powder and LPBF samples processed using different parameters.

Table 1. Effect of laser parameter on the TTs of LPBF-produced Ti-rich TiNi.

Specimens	**Heating**			**Cooling**		
	As (˚C)	**A_f (˚C)**	**E_A (J/g)**	**Ms (˚C)**	**M_f (˚C)**	**E_M (J/g)**
Powder	64	98	17.6	62	33	-18.4
67 J/mm^3	53	92	17.5	57	28	-17.9
133 J/mm^3	51	88	17.9	54	25	-17.5
267 J/mm^3	38	83	17.2	52	20	-16.9

4. Discussion

4.1. Laser process window analysis

As shown in Fig. 5, the formation of irregular pores was attributed to the turbulence in the melt pool at high P or E_v, or insufficient heat input leading to lack of fusion defects [14, 36]. An E_v as low as 44 J/mm^3 is apparently insufficient to achieve a complete solidification, which generated irregular pores. Additionally, as revealed in Fig. 4, low laser energy will also increase the tendency for balling. Generally, balling is caused by limited wetting due to the high surface tension of the melt pool. Low E_v melt pool reduces the wettability owing to the limited liquid metal in melt pool. It was reported that re-melting can suppress the balling [41]. It is possible that LPBF of lattice structures may have a higher tendency for balling than in solid structures due to the reduction in neighbouring laser tracks scans, which reduces the re-melting effect caused by the neighbouring laser scan. Balling increases the surface roughness and leads to more powder attachment to the surface of the struts, which compromises the geometrical integrity. In contrast, the spherical pores in high E_v processed samples (Fig. 5) were attributed to keyholing and Ni-evaporation [42], since the excessively high E_v up to 267 J/mm^3 increased the melt pool temperature and turbulence, causing material vaporisation combined with keyholing. As such, the build density increases initially with the increase in E_v to a threshold level beyond which it reduces with the increase in E_v. Besides, high E_v also increased the impurities pick-up, as plotted in Fig. 6b. Taking the above factors into consideration, a process map for Ti-rich LPBF-processed lattices was generated, Fig. 13. As illustrated in Fig. 13a, although the laser parameters in the red region reached the highest relative densities up to 99.76%, cracks formed along the build direction. Further increasing E_v or P aggravated the formation of cracks, as revealed in Fig. 13b. Only the low E_v ($\leq$ 110 J/mm^3) and low P ($\leq$75W) processed samples were crack-free.

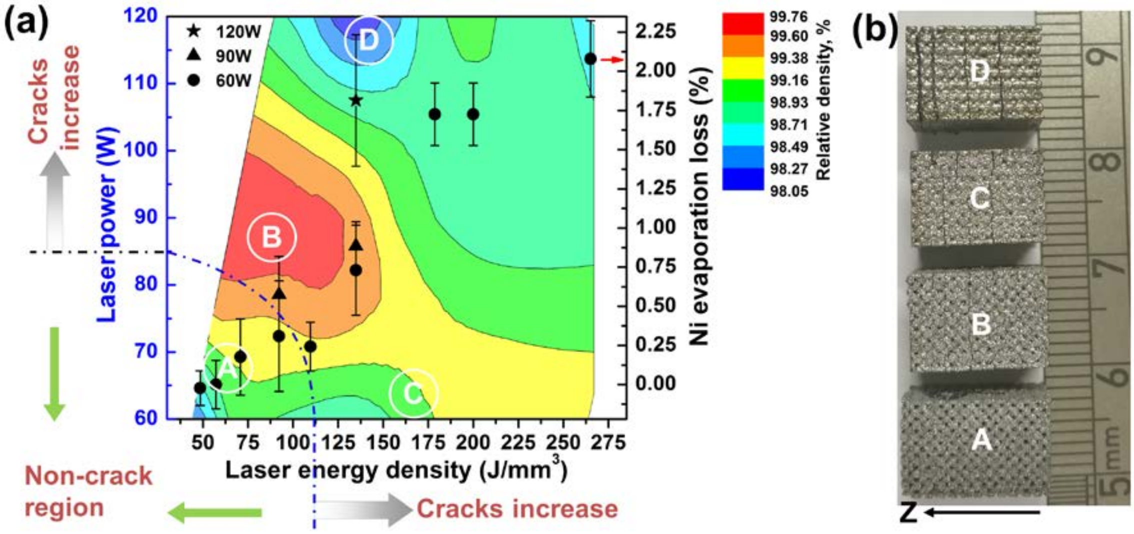

Fig. 13. Laser process map of LPBF-fabricated TiNi: (a) the effects of laser parameter on the relative density, Ni evaporation loss rate (right Y axis) and cracks of LPBF-processed samples; (b) macro appearance of representative samples taken from the four regions as circled by A-D in (a).

The rapid heating and subsequent cooling associated with LPBF leads to the formation of residual stresses due to the temperature gradient between the melt pools, causing cracks to form [43, 44]. The residual stresses are inevitable, but they could become more intense in higher power/energy conditions due to the elevated temperature gradient [45]. The Ni-loss %

(the % of the Ni at.% loss in the LPBF-processed TiNi samples to the original Ni at. % in powder), was also integrated into the process map Fig. 13a. Using either high E_v or P increased the Ni-loss %, with the highest loss approaching 2.1% at an E_v of 267 J/mm^3. Besides, high P also intensified Ni-loss dramatically (from about 0.7% to 1.8%) for the same E_v of 133J/mm^3. Though negligible, the higher Ni-loss can decrease the density of the LPBF-processed TiNi [16]. Moreover, higher E_v or P also increased the LTW and fusion boundary width, as shown in Fig. 7 and Fig. 4, which jeopardise the geometric integrity of lattice structures. Consequently, the optimum laser parameter window obtained in this work is considered to be E_v= 60-90 J/mm^3, alongside P= 60-75W, keeping the structural defects, densification, geometric resolution, Ni evaporation and impurity pick-up into consideration. The achievable relative density in this region is > 99%.

4.2. Geometrical control analysis

In order to ensure that the pore size achieves the design value, optimising the CD and BC is essential. Fig. 14 shows actual laser filling patterns generated in the Concept Laser M2 Cusing system when using different BC and CD values, and the correlative schematic illustrations of laser tracks further clarify the impact of the BC and CD. Understandably, when CD $\leq$0 (such as BC=CD=0 μm; and BC=0 μm, CD=-75μm), a reduced cavity size and an enlarged strut size will be created owing to the width of contour melt pool. When the difference between CD and BC is too large (e.g. at BC=0 μm and CD=75 μm), the filling scan will stretch over the contour scan, which impairs the function of the contour scan and results in poor surface finish. As observed in Fig. 8, using a BC=25 and without contour scan, a part with good geometrical precision can be built, the gap between the laser track boundary and defined part edge (i.e, BC=25 μm) is considered as metallurgical scaling regions. The surrounding surface of the cavity and strut are quite uneven, and the cavity shape is irregular without contour. In contrast, the surface roughness and cavity regularity in Fig. 9 were greatly improved when a contour scan was applied. Actually, the main function of using a contour scan in LPBF is to improve the surface finish. Therefore, using a contour scan in building porous or lattice structures using LPBF is indispensable.

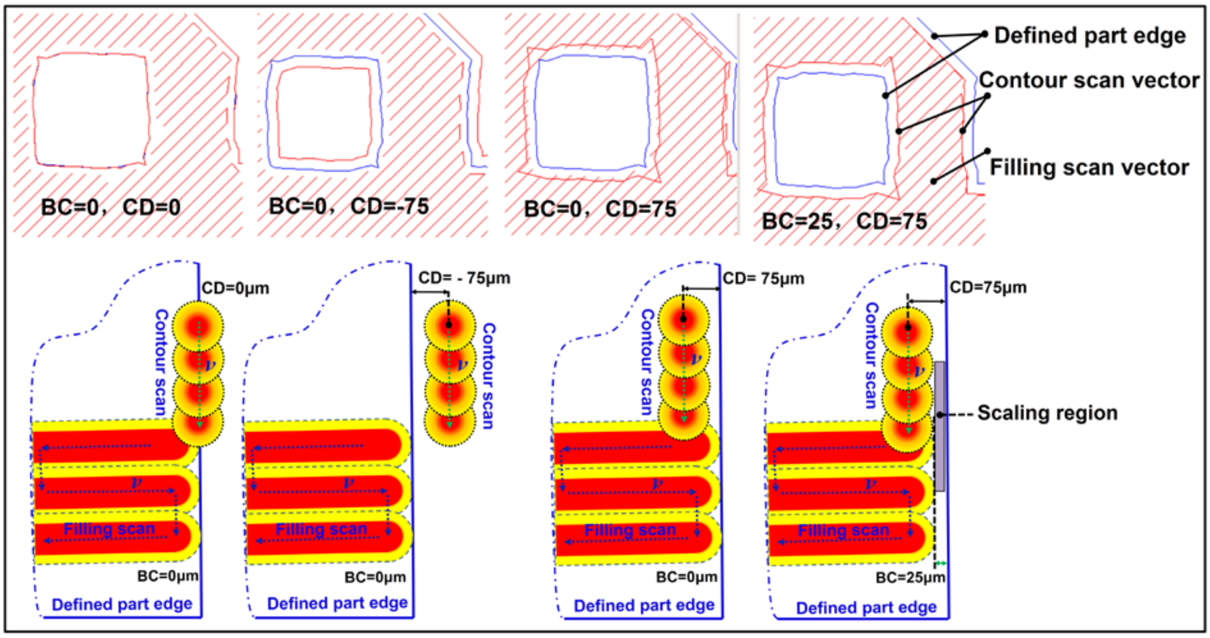

Fig. 14. Actual laser filling patterns generated in the Concept Laser M2 system and corresponding schematic illustrations of laser tracks using different beam compensation (BC) and contour distance (CD).

As illustrated in Fig. 14, when using the optimised BC value of 25 μm, a limited CD value (such as 0 μm) or minus CD value (such as -75 μm) could also reduce the cavity size, since the melt pool radius is larger and the laser track width of the contour scan track would beyond the defined part edge, which was demonstrated in Fig. 9a. When the gap between CD and BC is too large, such as BC=0 μm and CD=75 μm, the scan tracks will fill beyond the border of the contour tracks, which jeopardise the function of the contour scan. In Fig. 9b, the combination of BC =25μm and CD=75μm achieved the optimum geometrical precision, since the gap between the CD and BC (i.e., the CD-BC value of 50μm) is suitable for the contour scan filling up. Specifically, the LTW was measured as d=93±5 μm in Fig. 7 when E=67 J/mm^3 and P=60 W, meaning that half of the LTW (i.e, melt pool radius) was about 47 μm, which is quite close to the indicated 50 μm gap between CD and BC. In this case (i.e., CD - BC=1/2 × LTW), the surface finish and geometrical precision were all improved.

4.3. Phase transformation analysis

The variation in TTs associated with different E_v conditions (Fig. 12) can be attributed to the chemical variations associated with LPBF; mainly impurities (O and C) pick-up and Ni-loss. The relationship between oxygen content and M_S can be represented using the following empirical equation [46]:

$$M_S = 78 - 92.63\, x_O$$

where M_S is the martensite start temperature in ˚C and x_O is oxygen content in wt. %. Oxygen pick-up decreases the M_S by ~93 ˚C/wt.%, This decrease in M_S is related to the formation of Ti-rich secondary phases such as $Ti_4Ni_2O_X$, which in turn increases the Ni concentration in the matrix by withdrawing more Ti atoms [47, 48].

Carbon also decreases the TTs in TiNi through Ti-depletion by forming TiC, which would follow a quasi-binary eutectic reaction ($\mathrm{TiNiC} \xrightarrow{1280℃} \mathrm{TiNi}_{B2} + \mathrm{TiC}$) [49, 50]. Frenzel *et al.* [49] and Honma [46] investigated the effect of C on the martensitic phase transformations in TiNi SMAs. Frenzel *et al.* produced an empirical formula depicting the relationship between M_S (in ˚C) and the C concentration (x_c) in the TiNi alloy (in at.%) [49]:

$$M_s \approx 7.5℃ - 73.3 \frac{℃}{at.\%} \cdot x_c$$

So the M_S temperature can be decreased by about 73˚C/at.% by increasing the C-content according to the above relationship. Similarly, Honma [46] obtained a value of about 100˚C/at.%. Therefore, M_S can be lowered down to about 73-100 ˚C/at.% by increasing carbon content. This may be related to the fact that the TiC particles and its surrounding stress field promoted the nucleation and formation of martensite [49]. However, as shown in Fig. 6b, at a higher E_v, the C and O pick-up during LPBF process was <0.02 wt.% compared with the C and O contents in the as-received powder. These C and O pick-up amounts of <0.02 wt.% will be more even smaller (<<0.02 at.%) when using at. %, since the relative atomic mass of O and C are much smaller than Ni and Ti. Therefore, in our work, the influence of impurities pick-up during LPBF processes on the TTs was insignificant.

It is well known that the M_S, which is ~60° C in equiatomic TiNi, can be decreased continuously by approximately 83-100 ˚C per at.% with Ni addition [47, 48, 51]. But, when the Ni at.% content is lower than 50 at.%, the M_S is almost constant [48, 51]. However, the higher E_v input could result in a formation of a large amount of Ti_2Ni precipitates. One cannot neglect that the high Ti_2Ni content (18-27 vol.%) in this work (Fig. 11c) depleted a significant amount of Ti from the matrix, which may shift the TiNi matrix composition to a higher Ni. To verify this hypothesis, further calculations were conducted. The atomic percentage of TiNi and Ti_2Ni can be express as:

$$\frac{n_{Ti\mathrm{Ni}}}{n_{Ti2Ni}} = \frac{\rho_{Ti\mathrm{Ni}} V_{Ti\mathrm{Ni}}}{\rho_{Ti2\mathrm{Ni}} V_{Ti2\mathrm{Ni}}} \times \frac{M_{Ti2\mathrm{Ni}}}{M_{Ti\mathrm{Ni}}}$$

where $\rho_{Ti\mathrm{Ni}} = 6.49\ \mathrm{g/cm^3}$ and $\rho_{Ti2\mathrm{Ni}} = 5.72\ \mathrm{g/cm^3}$ [52, 53]. The molar mass of these two phases are $M_{Ti\mathrm{Ni}} = 107\mathrm{g/mol}$ and $M_{Ti2\mathrm{Ni}} = 155\mathrm{g/mol}$, respectively. So the ratio of ${n_{Ti\mathrm{Ni}}}/{n_{Ti2Ni}}$ was calculated to be 4.4-7.5 taking the Ti_2Ni content of 18-27 vol.% into consideration. On the basis that the atomic ratio of Ni:Ti in the raw powder was ~ 45.2:54.8 at.%, the atomic ratio of Ni:Ti in the TiNi matrix is calculated to be 49.6:50.4 at.% in low E_v (67J/mm^3) samples, and the atomic ratio of Ni:Ti in the matrix is 51:49 at.% in the higher E_v (267J/mm^3) samples. For the lower E_v sample (67J/mm^3), although, the Ti_2Ni precipitation caused Ni increase of matrix, the Ni content was still below 50 at.%, so the TTs was inclined to be stable despite the negligible decrease. As for the higher E_v sample (267J/mm^3), the increased Ni content (>50 at.%) could decrease TTs towards the region where it drops by 83-100 ˚C per at. % Ni increment in the matrix. Consequently, the main contribution to the TTs variation in the LPBF-processed samples could be the formation of Ti_2Ni intermetallic precipitates during LPBF processes, suggesting it is essential to perform post-LPBF heat treatment to homogenise the matrix chemistry and reduce the TiNi content, which will be discussed in our future publication, alongside the mechanical properties of the lattices.

5. Conclusions

LPBF was used to produce TiNi lattices with high-density (>99%) and high geometrical precision. The main findings can be summarised as follows:

(1) The optimum processing window identified in this work was E_v= 60-90 J/mm^3 along with P=60-75W by considering the impact of the process parameters on the formation of defects,

densification, geometrical precision, Ni-loss, and impurity pick-up into considerations. Higher E_v and P caused serious horizontal cracks and Ni evaporation.

(2) A reasonable combination of LTW, BC and CD, whereby CD - BC=1/2 × LTW, was critical to enable the geometry of the lattices to match the design.

(3) The solidified microstructure varied depending on the process parameters. The influence of impurities pick-up during the processes on the SME TTs was negligible, with the main contribution to the variation TTs being the high friction Ti_2Ni intermetallic precipitates that formed during the process, altering the TiNi matrix chemistry.

Data Sharing

The authors are happy to share the experimental data upon request.

References

[1] Bansiddhi A, Sargeant TD, Stupp SI, Dunand DC. Porous NiTi for bone implants: A review. Acta biomaterialia 2008;4:773-82.

[2] Taheri Andani M, Haberland C, Walker JM, Karamooz M, Sadi Turabi A, Saedi S, et al. Achieving biocompatible stiffness in NiTi through additive manufacturing. Journal of Intelligent Material Systems and Structures 2016;27:2661-71.

[3] Figueira N, Silva T, Carmezim M, Fernandes J. Corrosion behaviour of NiTi alloy. Electrochimica Acta 2009;54:921-6.

[4] Lexcellent C. Shape-memory alloys handbook: John Wiley & Sons; 2013.

[5] Dadbakhsh S, Speirs M, Van Humbeeck J, Kruth J-P. Laser additive manufacturing of bulk and porous shape-memory NiTi alloys: From processes to potential biomedical applications. MRS Bulletin 2016;41:765-74.

[6] Hartl DJ, Lagoudas DC. Aerospace applications of shape memory alloys. Proceedings of the Institution of Mechanical Engineers, Part G: Journal of Aerospace Engineering 2007;221:535-52.

[7] Ko J, Bhullar S, Cho Y, Lee PC, Jun MB-G. Design and fabrication of auxetic stretchable force sensor for hand rehabilitation. Smart Mater Struct 2015;24:075027.

[8] Elahinia MH, Hashemi M, Tabesh M, Bhaduri SB. Manufacturing and processing of NiTi implants: A review. Progress in materials science 2012;57:911-46.

[9] Wu S, Lin H, Chen C. A study on the machinability of a Ti49. 6Ni50. 4 shape memory alloy. Materials Letters 1999;40:27-32.

[10] Olakanmi EO, Cochrane RF, Dalgarno KW. A review on selective laser sintering/melting (SLS/SLM) of aluminium alloy powders: Processing, microstructure, and properties. Progress in Materials Science 2015;74:401-77.

[11] Tan C, Zhou K, Ma W, Attard B, Zhang P, Kuang T. Selective laser melting of high-performance pure tungsten: parameter design, densification behavior and mechanical properties. Science and Technology of Advanced Materials 2018:1-22.

[12] Li S, Hassanin H, Attallah MM, Adkins NJE, Essa K. The development of TiNi-based negative Poisson's ratio structure using selective laser melting. Acta Materialia 2016;105:75-83.

[13] Yan C, Hao L, Hussein A, Raymont D. Evaluations of cellular lattice structures manufactured using selective laser melting. International Journal of Machine Tools and Manufacture 2012;62:32-8.

[14] Saedi S, Shayesteh Moghaddam N, Amerinatanzi A, Elahinia M, Karaca HE. On the effects of selective laser melting process parameters on microstructure and thermomechanical response of Ni-rich NiTi. Acta Materialia 2018;144:552-60.

[15] Walker JM, Haberland C, Taheri Andani M, Karaca HE, Dean D, Elahinia M. Process development and characterization of additively manufactured nickel–titanium shape memory parts. Journal of Intelligent Material Systems and Structures 2016;27:2653-60.

[16] Haberland C, Elahinia M, Walker JM, Meier H, Frenzel J. On the development of high quality NiTi shape memory and pseudoelastic parts by additive manufacturing. Smart Materials and Structures 2014;23:104002.

[17] Shishkovsky I, Yadroitsev I, Smurov I. Direct selective laser melting of nitinol powder. Physics Procedia 2012;39:447-54.

[18] Bormann T, Müller B, Schinhammer M, Kessler A, Thalmann P, de Wild M. Microstructure of selective laser melted nickel–titanium. Materials Characterization 2014;94:189-202.

[19] Arabnejad S, Burnett Johnston R, Pura JA, Singh B, Tanzer M, Pasini D. High-strength porous biomaterials for bone replacement: A strategy to assess the interplay between cell morphology, mechanical properties, bone ingrowth and manufacturing constraints. Acta biomaterialia 2016;30:345-56.

[20] Pyka G, Burakowski A, Kerckhofs G, Moesen M, Van Bael S, Schrooten J, et al. Surface Modification of Ti6Al4V Open Porous Structures Produced by Additive Manufacturing. Advanced Engineering Materials 2012;14:363-70.

[21] de Wild M, Schumacher R, Mayer K, Schkommodau E, Thoma D, Bredell M, et al. Bone regeneration by the osteoconductivity of porous titanium implants manufactured by selective laser melting: a histological and micro computed tomography study in the rabbit. Tissue engineering Part A 2013;19:2645-54.

[22] Fujimoto K. An Experimental Study of Ti-Ni binary alloy as the material for implant. J Jpn Soc Oral Implant 1986;7:25-55.

[23] Muhonen V, Heikkinen R, Danilov A, Jämsä T, Tuukkanen J. The effect of oxide thickness on osteoblast attachment and survival on NiTi alloy. Journal of Materials Science: Materials in Medicine 2007;18:959-67.

[24] Mantovani D. Shape memory alloys: Properties and biomedical applications. Jom 2000;52:36-44.

[25] Shipley H, McDonnell D, Culleton M, Coull R, Lupoi R, O'Donnell G, et al. Optimisation of process parameters to address fundamental challenges during selective laser melting of Ti-6Al-4V: A review. International Journal of Machine Tools and Manufacture 2018;128:1-20.

[26] Lekston Z, Łągiewka E. X-ray diffraction studies of NiTi shape memory alloys. Archives of Materials Science and Engineering 2007;28:665-72.

[27] Wang X, Xu S, Zhou S, Xu W, Leary M, Choong P, et al. Topological design and additive manufacturing of porous metals for bone scaffolds and orthopaedic implants: A review. Biomaterials 2016;83:127-41.

[28] Karageorgiou V, Kaplan D. Porosity of 3D biomaterial scaffolds and osteogenesis. Biomaterials 2005;26:5474-91.

[29] Taniguchi N, Fujibayashi S, Takemoto M, Sasaki K, Otsuki B, Nakamura T, et al. Effect of pore size on bone ingrowth into porous titanium implants fabricated by additive manufacturing: An in vivo experiment. Materials science & engineering C, Materials for biological applications 2016;59:690-701.

[30] Hassanin H, Finet L, Cox SC, Jamshidi P, Grover LM, Shepherd DET, et al. Tailoring selective laser melting process for titanium drug-delivering implants with releasing micro-channels. Additive Manufacturing 2018;20:144-55.

[31] Zhou X, Liu X, Zhang D, Shen Z, Liu W. Balling phenomena in selective laser melted tungsten. Journal of Materials Processing Technology 2015;222:33-42.

[32] Tan C, Zhou K, Kuang M, Ma W, Kuang T. Microstructural characterization and properties of selective laser melted maraging steel with different build directions. Science and Technology of Advanced Materials 2018;19:746-58.

[33] Liu YJ, Li SJ, Wang HL, Hou WT, Hao YL, Yang R, et al. Microstructure, defects and mechanical behavior of beta-type titanium porous structures manufactured by electron beam melting and selective laser melting. Acta Materialia 2016;113:56-67.

[34] Qiu C, Yue S, Adkins NJE, Ward M, Hassanin H, Lee PD, et al. Influence of processing conditions on strut structure and compressive properties of cellular lattice structures fabricated by selective laser melting. Materials Science and Engineering: A 2015;628:188-97.

[35] Kou S. Welding Metallurgy. 2nd ed. New York: Wiley; 2003.

[36] Tan C, Zhou K, Ma W, Min L. Interfacial characteristic and mechanical performance of maraging steel-copper functional bimetal produced by selective laser melting based hybrid manufacture. Materials & Design 2018;155:77-85.

[37] Li R, Liu J, Shi Y, Wang L, Jiang W. Balling behavior of stainless steel and nickel powder during selective laser melting process. The International Journal of Advanced Manufacturing Technology 2012;59:1025-35.

[38] Tan C, Zhou K, Ma W, Zhang P, Liu M, Kuang T. Microstructural evolution, nanoprecipitation behavior and mechanical properties of selective laser melted high-performance grade 300 maraging steel. Materials & Design 2017;134:23-34.

[39] Ataee A, Li Y, Brandt M, Wen C. Ultrahigh-strength titanium gyroid scaffolds manufactured by selective laser melting (SLM) for bone implant applications. Acta Materialia 2018;158:354-68.

[40] Doubenskaia M, Domashenkov A, Smurov I, Petrovskiy P. Study of Selective Laser Melting of intermetallic TiAl powder using integral analysis. International Journal of Machine Tools and Manufacture 2018;129:1-14.

[41] Yap CY, Chua CK, Dong ZL, Liu ZH, Zhang DQ, Loh LE, et al. Review of selective laser melting: Materials and applications. Applied Physics Reviews 2015;2:041101.

[42] Qiu C, Panwisawas C, Ward M, Basoalto HC, Brooks JW, Attallah MM. On the role of melt flow into the surface structure and porosity development during selective laser melting. Acta Materialia 2015;96:72-9.

[43] Kruth J-P, Dadbakhsh S, Vrancken B, Kempen K, Vleugels J, Van Humbeeck J. Additive manufacturing of metals via Selective Laser Melting: Process aspects and material developments. 2015.

[44] Song B, Zhao X, Li S, Han C, Wei Q, Wen S, et al. Differences in microstructure and properties between selective laser melting and traditional manufacturing for fabrication of metal parts: A review. Frontiers of Mechanical Engineering 2015;10:111-25.

[45] Mercelis P, Kruth JP. Residual stresses in selective laser sintering and selective laser melting. Rapid Prototyping Journal 2006;12:254-65.

[46] Honma T. Shape Memory Alloys, ed. by H. Funakubo,(New York, Gordon and Breach Science Publishers, 1987) pp 1987:61-115.

[47] Khalil-Allafi J, Dlouhy A, Eggeler G. Ni4Ti3-precipitation during aging of NiTi shape memory alloys and its influence on martensitic phase transformations. Acta Materialia 2002;50:4255-74.

[48] Tang W, Sundman B, Sandström R, Qiu C. New modelling of the B2 phase and its associated martensitic transformation in the Ti–Ni system. Acta materialia 1999;47:3457-68.

[49] Frenzel J, Zhang Z, Somsen C, Neuking K, Eggeler G. Influence of carbon on martensitic phase transformations in NiTi shape memory alloys. Acta Materialia 2007;55:1331-41.

[50] Bandyopadhyay D, Sharma R, Chakraborti N. The Ti-Ni-C system (titanium-nickel-carbon). Journal of phase equilibria 2000;21:186.
[51] Frenzel J, George EP, Dlouhy A, Somsen C, Wagner MFX, Eggeler G. Influence of Ni on martensitic phase transformations in NiTi shape memory alloys. Acta Materialia 2010;58:3444-58.
[52] Michal G, Sinclair R. The structure of TiNi martensite. Acta Crystallographica Section B 1981;37:1803-7.
[53] Yurko G, Barton J, Parr JG. The crystal structure of Ti2Ni. Acta Crystallographica 1959;12:909-11.